Documentation - CTE2014

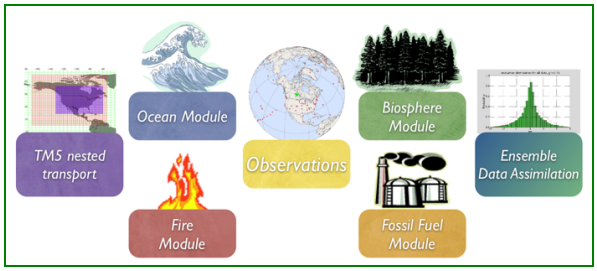

To learn more about a CarbonTracker component, click on one of the above images.
Or **download the full PDF version** for convenience.

Oceans Module [go to top]

1. Introduction

The oceans play an important role in the Earth's carbon cycle. They are the largest long-term sink for carbon and have an enormous capacity to store and redistribute CO_2 within the system. Oceanographers estimate that about 48% of the CO_2 from fossil fuel burning has been absorbed by the ocean [Sabine et al., 2004]. The dissolution of CO_2 in seawater shifts the balance of the ocean carbonate equilibrium towards a more acidic state (i.e., with a lower pH). This effect is already measurable [Caldeira and Wickett, 2003], and is expected to become an acute challenge to shell-forming organisms over the coming decades and centuries. Although the oceans as a whole have been a relatively steady net carbon sink, CO_2 can also come out of the oceans depending on local temperatures, biological activity, wind speeds, and ocean circulation. These processes are all considered in CarbonTracker, since they can have significant effects on the ocean sink. Improved estimates of the air-sea exchange of carbon in turn help us to understand variability of both the atmospheric burden of CO_2 and terrestrial carbon exchange.

2. Detailed Description

Oceanic uptake of CO_2 in CarbonTracker is computed using air-sea differences in partial pressure of CO_2 inferred from ocean inversions, combined with a gas transfer velocity computed from wind speeds in the atmospheric transport model.

The long-term mean air-sea fluxes, and the uncertainties associated with them, derive from the ocean interior inversions reported in Jacobson et al. [2007]. These ocean inversion flux (OIF) estimates are composed of separate preindustrial (natural) and anthropogenic flux inversions based on the methods described in Gloor et al. [2003] and biogeochemical interpretations of Gruber, Sarmiento, and Stocker [1996]. The uptake of anthropogenic CO_2 by the ocean is assumed to increase in proportion to atmospheric CO_2 levels, consistent with estimates from ocean carbon models.

For CarbonTracker Europe, contemporary pCO_2 fields were computed by summing the preindustrial and anthropogenic flux components from inversions using five different configurations of the Princeton/GFDL MOM3 ocean general circulation model [Pacanowski and Gnanadesikan, 1998], then dividing by a gas transfer velocity computed from the European Centre for Medium-Range Weather Forecasts (ECMWF) ERA40 reanalysis. There are two small differences in first-guess fluxes in this computation from those reported in Jacobson et al. [2007]. First, the five OIF estimates all used Takahashi et al. [2002] pCO_2 estimates to provide high-resolution patterning of flux within inversion regions (the alternative "forward" model patterns were not used). To good approximation, this choice only affects the spatial and temporal distribution of flux within each of the **30 ocean inversion regions**, not the magnitude of the estimated flux. Second, wind speed differences between the ERA40 product used in the offline analysis and the ECMWF operational model used in the online CarbonTracker analysis result in small deviations from the OIF estimates.

Gas transfer velocity in CarbonTracker is parameterized as a quadratic function of wind speed following Wanninkhof [1992], using the formulation for instantaneous winds. Gas exchange is computed every 3 hours using wind speeds from the ECMWF operational model as represented by the **TM5 atmospheric transport model**. Other than the smooth trend in anthropogenic flux assumed by the OIF results, interannual variability (IAV) in the first guess ocean flux comes entirely from wind speed effects on the gas transfer velocity. This is because the ocean inversions retrieve only a long-term mean and smooth trend.

The initial release of CarbonTracker (2007A) used climatogical estimates of CO_2 partial pressure in surface waters from Takahashi et al. [2002] to compute a first-guess air-sea flux. This air-sea pCO_2 disequilibrium was modulated by a surface barometric pressure correction before being multiplied by a gas-transfer coefficient to yield a flux. Starting with CarbonTracker 2007B and in this CarbonTracker Europe release, the air-sea pCO_2 disequilibrium is imposed from analysis of the OIF results, with short-term flux variability derived from the atmospheric model wind speeds via the gas transfer coefficient. The barometric pressure correction has been removed so that climatological high- and low-pressure cells do not bias the long-term means of the first guess fluxes. In either method, the first-guess fluxes have no interannual variability (IAV) due to pCO_2 changes, such as those that occur in the tropical eastern Pacific during an El Niño. In CarbonTracker, this flux IAV must be inferred from atmospheric CO_2 signals.

Air-sea transfer is inhibited by the presence of sea ice, and for this work fluxes are scaled by the daily sea ice fraction in each gridbox provided by the ECMWF forecast data.

The first-guess fluxes described here are subject to scaling during the CarbonTracker optimization process, in which atmospheric CO_2 mole fraction observations are combined with transport simulated by the atmospheric model to infer flux signals. In this process, signals of terrestrial flux in atmospheric CO_2 distribution can be erroneously interpreted as being caused by oceanic fluxes. This flux "aliasing" or "leakage" is evident in some regions as a change in the shape of the seasonal cycle of air-sea flux. Differences between CarbonTracker posterior air-sea fluxes and those of the OIF prior fluxes are minor, but do constitute an issue that we will be investigating in the future.

3. Further Reading

- **NOAA Pacific Marine Environmental Laboratory (PMEL)**
- **Ocean Acidification**

- Caldeira, K., and M. E. Wickett (2003), Anthropogenic carbon and ocean pH, Nature, 425365-365.
- Gloor, M., N. Gruber, J. Sarmiento, C. L. Sabine, R. A. Feely, and C. RÃ¶beck (2003), A first estimate of present and preindustrial air-sea CO_2 flux patterns based on ocean interior carbon measurements and models, Geophysical Research Letters, 30, , 10.1029/2002GL015594.
- Gruber, N., J. L. Sarmiento, and T. F. Stocker (1996), An improved method for detecting anthropogenic CO_2 in the oceans, Global Biogeochemical Cycles, 10, , 809-837.
- Jacobson, A. R., N. Gruber, J. L. Sarmiento, M. Gloor, and S. E. Mikaloff Fletcher (2007), A joint atmosphere-ocean inversion for surface fluxes of carbon dioxide: I. Methods and global-scale fluxes, Global Biogeochemical Cycles, 21, doi:10.1029/2005GB002556.
- Pacanowski, R. C., and A. Gnanadesikan (1998), Transient response in a z-level ocean model that resolves topography with partial cells, Monthly Weather Review, 126, 3248--3270.
- Sabine, C. L., R. A. Feely, N. Gruber, R. M. Key, K. Lee, J. L. Bullister, R. Wanninkhof, C. S. Wong, D. W. R. Wallace, B. Tilbrook, F. J. Millero, T. H. Peng, A. Kozyr, T. Ono, and A. F. Rios (2004), The oceanic sink for anthropogenic CO_2, Science, 305, 367-371.
- Takahashi, T., S. C. Sutherland, C. Sweeney, A. P. N. Metzl, B. Tilbrook, N. Bates, R. Wanninkhof, R. A. Feely, C. Sabine, J. Olafsson, and Y. Nojiri (2002), Global air-sea CO_2 flux based on climatological surface ocean pCO_2, and seasonal biological and temperature effects, Deep-Sea Research II, 49, , 1601--1622.
- Wanninkhof, R. (1992), Relationship between wind speed and gas exchange over the ocean, Journal of Geophysical Research, 97, 7373--7382.

Biosphere Module [go to top]

1. Introduction

The biospheric component of the carbon cycle consists of all the carbon stored in 'biomass' around us. This includes trees, shrubs, grasses, carbon within soils, dead wood, and leaf litter. Such reservoirs of carbon can exchange CO_2 with the atmosphere. Exchange starts when plants take up CO_2 during their growing season through the process called photosynthesis (uptake). Most of this carbon is released back to the atmosphere throughout the year through a process called respiration (release). This includes both the decay of dead wood and litter and the metabolic respiration of living plants. Of course, plants can also return carbon to the atmosphere when they burn, **as described here**. Even though the yearly sum of uptake and release of carbon amounts to a relatively small number (a few petagrams (one $Pg=10^{15}$ g)) of carbon per year, the flow of carbon each way is as large as 120 Pg each year. This is why the net result of these flows needs to be monitored in a system such as ours. It is also the reason we need a good physical description (model) of these flows of carbon. After all, from the atmospheric measurements we can only see the small net sum of the large two-way streams (gross fluxes). Information on what the biospheric fluxes are doing in each season, and in every location on Earth is derived from a specialized biosphere model, and fed into our system as a first guess, to be refined by our assimilation procedure.

2. Detailed Description

The biosphere model currently used in CarbonTracker is the Simple-Biosphere-Model-Carnegie-Ames Stanford Approach (SiBCASA) biogeochemical model. This model calculates global carbon fluxes using input from weather models to drive biophysical processes, as well as satellite observed Normalized Difference Vegetation Index (NDVI) to track plant phenology. The version of SiBCASA model output used so far was driven by year specific weather and satellite observations, and including the effects of fires on photosynthesis and respiration (see van der Velde et al., [2014], van der Werf et al., [2006] and Giglio et al., [2006]). This simulation gives 1x1 degree global fluxes on a 10-minute time resolution, which we average to monthly means for further processing.

Net Ecosystem Exchange (NEE) is derived from the monthly mean SiBCASA Gross Primary Production (GPP) and ecosystem respiration (R_E). Higher frequency variations (diurnal, synoptic) are added to GPP and R_E fluxes every 3 hours using a simple temperature Q_{10} relationship assuming a global Q_{10} value of 1.5 for respiration, and a linear scaling of photosynthesis with solar radiation. The procedure is very similar, but **NOT** identical to the procedure in Olsen and Randerson [2004] and based on ECMWF analyzed meteorology. Note that the introduction of 3-hourly variability conserves the monthly mean NEE from the SiBCASA model. Instantaneous NEE for each 3-hour interval is thus created as:

$$NEE(t) = GPP(I, t) + R_E(T, t)$$

$$GPP(t) = I(t) * (\Sigma(GPP) / \Sigma(I))$$

$$R_E(t) = Q_{10}(t) * (\Sigma(R_E) / \Sigma(Q_{10}))$$

$$Q_{10}(t) = 1.5^{((T_{2m}-T_0) / 10.0)}$$

where T=2 meter temperature, I=incoming solar radiation, t=time, and summations are done over one month in time, per gridbox. The instantaneous fluxes yielded realistic diurnal cycles when used in the TransCom Continuous experiment.

Between September 2012 and December 2013 we used climatological mean values.

3. Further Reading

- **van der Velde, I. R. *et al.* (2013)**, Biosphere model simulations of interannual variability in terrestrial $^{13}C/^{12}C$ exchange, *Global Biogeochemical Cycles*, 27(3), 637–649.
- **van der Velde, I. R. *et al.* (2014)**, Terrestrial cycling of $^{13}CO_2$ by photosynthesis, respiration, and biomass burning in SiBCASA , *Biogeosciences*, 11, 6553–6571.
- **Schaefer, K. *et al.* (2008)**, Combined simple biosphere/Carnegie–Ames–Stanford approach terrestrial carbon cycle model. *Journal of Geophysical Research: Atmospheres* , 113(G3)
- **Olsen and Randerson (2004)**, Differences between surface and column atmospheric CO_2 and implications for carbon cycle research, *Journal of Geophysical Research: Atmospheres*, 109, D2, 27
- **van der Werf, G.R. *et al.* (2006)**, Interannual variability in global biomass burning emissions from 1997 to 2004, *Atm. Chem. Phys.*, 6(11), 3423–3441

Fire Module [go to top]

1. Introduction

Vegetation fires are an important part of the carbon cycle and have been so for many millennia. Even before human civilization began to use fires to clear land for agricultural purposes, most ecosystems were subject to natural wildfires that would rejuvenate old forests and bring important minerals to the soils. When fires consume part of the landscape in either controlled or natural burning, carbon dioxide (amongst many other gases and aerosols) is released in large quantities. Each year, vegetation fires emit more than 2 PgC as CO_2 into the atmosphere, mostly in the tropics. Currently, a large fraction of these fires is started by humans, and mostly intentionally to clear land for agriculture, or to re-fertilize soils before a new growing season. This important component of the carbon cycle is monitored mostly from space, while sophisticated 'biomass burning' models are used to estimate the amount of CO_2 emitted by each fire. Such estimates are then used in CarbonTracker to prescribe the emissions, without further refinement by our measurements.

2. Detailed Description

The fire module currently used in CarbonTracker is based on the Global Fire Emissions Database version 4 (GFEDv4), which is used in the SiBCASA biosphere model as described **here**. The GFED4 dataset consists of 0.25x0.25 degree gridded monthly burned area for the time period spanning January 1997 - August 2012. The CO_2 emissions are calculated in SiBCASA using the Burned Area and the vegetation types. The GFEDv4 burned area is based on MODIS satellite observations of fire counts. The full data set was produced by combining 500 m MODIS burned area maps with active fire data from the Tropical Rainfall Measuring Mission (TRMM) Visible and Infrared Scanner (VIRS) and the Along-Track Scanning Radiometer (ATSR) family of sensors.

Once burned area has been estimated globally, emissions of trace gases are calculated using the SiBCASA biosphere model. The seasonally changing vegetation and soil biomass stocks in the SiBCASA model are combusted based on the burned area estimate, and converted to atmospheric trace gases using estimates of fuel loads, combustion completeness, and burning efficiency. Between September 2012 and December 2013 we used climatological mean values.

GFED products were successfully used in recent studies of CH_4, CO_2, CO, and other trace gases.

3. Further Reading

- **Giglio, L. *et al.* (2013)**, Analysis of daily, monthly, and annual burned area using the fourth-generation global fire emissions database (GFED4), *J. Geophys. Res.: Biogeosciences*, 118, 317–328
- **van der Werf, G. R. *et al.* (2006)**, Interannual variability in global biomass burning emissions from 1997 to 2004, *Atm. Chem. Phys.*, 6(11), 3423–3441
- **van der Velde, I. R. *et al.* (2013)**, Biosphere model simulations of interannual variability in terrestrial $^{13}C/^{12}C$ exchange, *Global Biogeochemical Cycles*, 27(3), 637–649.
- **van der Velde, I. R. *et al.* (2014)**, Terrestrial cycling of $^{13}CO_2$ by photosynthesis, respiration, and biomass burning in SiBCASA , *Biogeosciences*, 11, 6553–6571.
- **Giglio *et al.* (2006)**, Global estimation of burned area using MODIS active fire observations, Atmos. Chem. Phys., 6, 957–974

Observations [go to top]

1. Introduction

The observations of CO_2 mole fraction by NOAA ESRL and partner laboratories are at the heart of CarbonTracker. They inform us on changes in the carbon cycle, whether they are regular (such as the seasonal growth and decay of leaves and trees), or irregular (such as the release of tons of carbon by a wildfire). The results in CarbonTracker depend directly on the quality, amount and location of observations available, and the degree of detail at which we can monitor the carbon cycle reliably increases strongly with the density of our observing network.

2. Detailed Description

This study uses CO_2 measurements of air samples collected at 96 global sites by several institutions worldwide. All contributing laboratories are included under **collaborators**. These observations are included in **ObsPack** PROTOTYPEv1.0.3, PROTOTYPEv1.0.4b and NOAA-DATAv1.0. These ObsPack contains 188 time series of surface flask samples, quasi-continuous in-situ observations also from towers and aircraft samples. Table 1 and the figure below summarize which time series have been used in our inversion. We assimilate only 1 time series per site (e.g. not 2 from the same location from different laboratories). Note that all of these observations are calibrated against the same world CO_2 scale (WMO-2007).

For most of the quasi-continuous sampling sites, the time series consist of an afternoon daytime average mole fraction for each day from the time series, recognizing that our atmospheric transport model does not always capture the continental nighttime stability regime while daytime well-mixed conditions are better matched. At mountain-top sites (e.g. MLO, NWR, and SPL), we use an average of nighttime hours as this tends to be the most stable time period and avoids periods of upslope flows that contain local vegetative and/or anthropogenic influence. Moreover, observations at sub-daily time scales are likely to be strongly correlated and therefore add relatively little independent information to our results. Also based on Transcom continuous simulations, we decided to move a set of coastal sites by one degree into the ocean to force the model sample to be more representative of the actual site conditions. Table 1 summarizes how data from the different measurement programs are included for this study.

The CO_2 data from ObsPack used in CarbonTracker are freely available for **download**. Users are encouraged to review the literature and contact the measurement labs directly for details about and access to the actual observations.

We apply a further selection criterion during the assimilation to exclude non-marine boundary layer (MBL) and deep Southern Hemisphere observations that are very poorly forecasted in our framework. We use the so-called model-data mismatch in this process, which is the random error ascribed to each observation to account for measurement errors as well as modeling errors of that observation. We interpret an observed-minus-forecasted (OmF) mole fraction that exceeds 3 times the prescribed model-data mismatch as an indicator that our modeling framework fails. This can happen for instance when an air sample is representative of local exchange not captured well by our 1x1 degree fluxes, when local meteorological conditions are not captured by our offline transport fields, but also when large-scale CO_2 exchange is suddenly changed (e.g. fires, pests, droughts) to an extent that can not be accommodated by our flux modules. This last situation would imply an important change in the carbon cycle and has to be recognized by the researchers when analyzing the results. In accordance with the 3-sigma rejection criterion, ~2% of the observations are discarded through this mechanism in our assimilations.

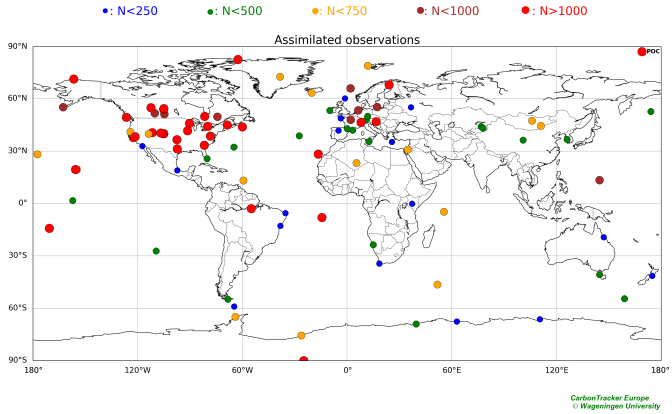

Table 1 gives a summary of the observing sites used in CarbonTracker and the assimilation performance. Model-data-mismatch ("R") is a value assigned to a given site that is meant to quantify our expected ability to simulate observations there. This value is principally determined from the limitations of the atmospheric transport model. It is part of the standard deviation used to interpret the difference between a simulation first guess ("Hx") of an observation and the actual measured value ("z"). The other component, HPH^T is a measure of the ability of the ensemble Kalman filter to improve its simulated value for this observation by adjusting fluxes. These elements together form the innovation χ statistic for the site: $\chi = (z-Hx)/\sqrt{(HPH^T+r^2)}$. The innovation χ^2 reported above is the mean of all squared χ values for a given site. An average χ^2 below 1.0 indicates that the $\sqrt{(HPH^T+r^2)}$ values are too large. Conversely, values above 1.0 mean that this standard deviation is underestimated. The bias is a statistic of the posterior residuals (final modeled values - measured values). The bias is the mean of these residuals.

Table 1: Summary of observing sites used in CarbonTracker Europe and assimilation performance.

Site code	Sampling Type	Lab.	Country	Lat, Lon, Elev. (m ASL)	No. Obs. Avail.	√R (µmol mol^{-1})	√HPH (µmol mol^{-1})	H(x)-y (µmol mol^{-1})	H(x)-y (JJAS) (µmol mol^{-1})	H(x)-y (NDJFMA) (µmol mol^{-1})	Inn. χ^2	Site code
ABP	surface-flask	NOAA	Brazil	12°46'S, 38°10'W, 1 masl	101	+1.50	+0.49	-0.70± 0.79	-0.17± 0.45	-1.17± 0.74	+0.59	ABP
ABP	surface-flask	IPEN	Brazil	12°46'S, 38°10'W, 1 masl	104	+1000.00	+0.50	-1.00± 1.37	-0.43± 1.22	-1.50± 1.26	-99.00	ABP

ALT	surface-flask	NOAA	Canada	82°27'N, 62°30'W, 200 masl	623	+1000.00	+0.52	+0.18± 0.80	-0.06± 1.03	+0.36± 0.62	-99.00	ALT
ALT	surface-flask	CSIRO	Canada	82°27'N, 62°30'W, 200 masl	366	+1000.00	+0.52	+0.16± 0.81	-0.02± 0.93	+0.36± 0.72	-99.00	ALT
ALT	surface-flask	SIO	Canada	82°27'N, 62°30'W, 200 masl	268	+1000.00	+0.50	+0.35± 0.77	+0.09± 0.98	+0.56± 0.61	-99.00	ALT
ALT	surface-insitu	EC	Canada	82°27'N, 62°30'W, 200 masl	3957	+1.50	+0.50	+0.19± 0.75	+0.04± 0.91	+0.30± 0.67	+0.38	ALT
AMT	surface-pfp	NOAA	United States	45° 2'N, 68°41'W, 53 masl	738	+1000.00	+5.65	-0.14± 3.48	-0.12± 5.38	-0.25± 2.25	-99.00	AMT
AMT	tower-insitu	NOAA	United States	45° 2'N, 68°41'W, 53 masl	2666	+4.00	+6.00	+0.12± 2.41	+0.70± 3.13	-0.27± 1.78	+0.32	AMT
AOA	aircraft-flask	JMA	Japan	99°60'S, 999°60'W, -9999 masl	239	+1000.00	+0.16	+0.67± 0.96	+0.46± 1.18	+0.96± 0.73	-99.00	AOA
ARA	surface-flask	CSIRO	Australia	23°52'S, 148°28'E, 175 masl	1	+1000.00	+0.55	+0.06± 0.00	+0.06± 0.00	+nan± nan	-99.00	ARA
ASC	surface-flask	NOAA	United Kingdom	7°58'S, 14°24'W, 85 masl	1083	+0.75	+0.21	-0.06± 0.72	+0.35± 0.66	-0.39± 0.63	+1.04	ASC
ASK	surface-flask	NOAA	Algeria	23°11'N, 5°25'E, 1842 masl	559	+0.75	+0.15	+0.10± 0.66	+0.00± 0.65	+0.20± 0.67	+0.81	ASK
AZR	surface-flask	NOAA	Portugal	38°46'N, 27°23'W, 19 masl	326	+1.50	+0.50	+0.26± 1.31	+0.45± 1.42	+0.24± 1.25	+0.81	AZR
BAL	surface-flask	NOAA	Poland	55°21'N, 17°13'E, 3 masl	885	+5.00	+5.09	-0.67± 3.20	-0.78± 3.50	-0.59± 3.09	+0.43	BAL
BAO	surface-pfp	NOAA	United States	40° 3'N, 105° 0'W, 1584 masl	1234	+1000.00	+1.13	-2.06± 4.62	-0.72± 2.69	-2.96± 5.44	-99.00	BAO
Site code	**Sampling Type**	**Lab.**	**Country**	**Lat, Lon, Elev. (m ASL)**	**No. Obs. Avail.**	**√R (µmol mol⁻¹)**	**√HPH (µmol mol⁻¹)**	**H(x)-y (µmol mol⁻¹)**	**H(x)-y (JJAS) (µmol mol⁻¹)**	**H(x)-y (NDJFMA) (µmol mol⁻¹)**	**Inn. X^2**	**Site code**
BAO	tower-insitu	NOAA	United States	40° 3'N, 105° 0'W, 1584 masl	1469	+3.00	+1.15	-1.14± 2.51	-0.53± 2.19	-1.73± 2.60	+0.92	BAO
BAO	tower-insitu	NOAA	United States	40° 3'N, 105° 0'W, 1584 masl	1512	+1000.00	+8.85	+3.18± 9.44	+3.42±12.10	+3.79± 7.54	-99.00	BAO
BCK	surface-insitu	EC	Canada	62°48'N, 116° 3'W, 179 masl	271	+1000.00	+3.19	+0.28± 3.38	-1.82± 4.25	+1.45± 2.37	-99.00	BCK
BGI	aircraft-pfp	NOAA	United States	42°49'N, 94°25'W, 355 masl	357	+1000.00	+2.86	+0.15± 2.92	-0.15± 4.04	+0.36± 1.38	-99.00	BGI
BGU	surface-flask	LSCE	Spain	41°58'N, 3°14'E, 11 masl	374	+2.50	+3.84	+0.08± 2.18	+0.38± 2.03	+0.05± 2.23	+0.82	BGU
BHD	surface-flask	NOAA	New Zealand	41°25'S, 174°52'E, 85 masl	172	+0.75	+0.26	+0.22± 0.70	+0.58± 0.73	-0.02± 0.62	+1.04	BHD
BKT	surface-flask	NOAA	Indonesia	0°12'S, 100°19'E, 845 masl	284	+1000.00	+1.33	+2.45± 4.23	+1.89± 4.99	+2.72± 3.95	-99.00	BKT
BME	surface-flask	NOAA	United Kingdom	32°22'N, 64°39'W, 12 masl	192	+1.50	+0.61	+0.46± 1.27	+1.13± 1.33	+0.17± 1.23	+0.92	BME
BMW	surface-flask	NOAA	United Kingdom	32°16'N, 64°53'W, 30 masl	415	+1.50	+0.68	+0.48± 1.03	+0.60± 0.98	+0.41± 1.00	+0.61	BMW
BNE	aircraft-pfp	NOAA	United States	40°48'N, 97°11'W, 465 masl	1080	+1000.00	+2.43	+0.27± 3.27	+0.70± 3.81	+0.35± 1.65	-99.00	BNE
BRA	surface-insitu	EC	Canada	51°12'N, 104°42'W, 595 masl	867	+3.00	+6.18	-0.05± 2.02	+0.13± 2.42	-0.10± 1.80	+0.47	BRA
BRW	surface-flask	NOAA	United States	71°19'N, 156°37'W, 11 masl	594	+1000.00	+1.38	+0.22± 1.33	+0.44± 1.95	+0.14± 0.90	-99.00	BRW
BRW	surface-insitu	NOAA	United States	71°19'N, 156°37'W, 11 masl	3158	+1.50	+1.11	+0.28± 0.79	+0.29± 1.04	+0.27± 0.64	+0.51	BRW
BSC	surface-flask	NOAA	Romania	44°11'N, 28°40'E, 0 masl	389	+1000.00	+4.69	-6.03± 9.33	-10.31±11.21	-3.51± 6.58	-99.00	BSC
CAR	aircraft-pfp	NOAA	United States	40°22'N, 104°18'W, 1740 masl	4132	+1000.00	+0.52	+0.48± 1.12	+0.44± 1.47	+0.51± 0.80	-99.00	CAR
Site code	**Sampling Type**	**Lab.**	**Country**	**Lat, Lon, Elev. (m ASL)**	**No. Obs. Avail.**	**√R (µmol mol⁻¹)**	**√HPH (µmol mol⁻¹)**	**H(x)-y (µmol mol⁻¹)**	**H(x)-y (JJAS) (µmol mol⁻¹)**	**H(x)-y (NDJFMA) (µmol mol⁻¹)**	**Inn. X^2**	**Site code**
CBA	surface-flask	NOAA	United States	55°13'N, 162°43'W, 21 masl	852	+1.50	+0.65	-0.32± 1.43	+0.76± 1.64	-0.84± 0.95	+1.08	CBA
CBA	surface-flask	SIO	United States	55°13'N, 162°43'W, 21 masl	250	+1000.00	+0.64	+0.26± 2.00	+1.46± 2.80	-0.23± 0.93	-99.00	CBA
CBY	surface-insitu	EC	Canada	69° 1'N, 105° 3'W, 35 masl	23	+1000.00	+2.43	+nan± nan	+nan± nan	+nan± nan	-99.00	CBY
CDL	surface-insitu	EC	Canada	53°59'N, 105° 7'W, 600 masl	2752	+3.00	+9.15	+0.15± 1.69	+0.43± 2.22	+0.02± 1.41	+0.34	CDL
CFA	surface-flask	CSIRO	Australia	19°17'S, 147° 4'E, 2 masl	219	+1.50	+0.70	-0.55± 1.00	-0.32± 1.12	-0.76± 0.91	+0.59	CFA
CGO	surface-flask	NOAA	Australia	40°41'S, 144°41'E, 94 masl	442	+0.50	+0.12	+0.18± 0.37	+0.47± 0.29	-0.05± 0.28	+0.71	CGO
CGO	surface-flask	CSIRO	Australia	40°41'S, 144°41'E, 94 masl	408	+1000.00	+0.12	+0.16± 0.35	+0.41± 0.27	-0.07± 0.26	-99.00	CGO
CGO	surface-flask	SIO	Australia	40°41'S, 144°41'E, 94 masl	253	+1000.00	+0.13	+0.39± 0.39	+0.66± 0.33	+0.15± 0.27	-99.00	CGO
CHM	surface-insitu	EC	Canada	49°41'N, 74°18'W, 393 masl	944	+3.00	+3.56	+0.04± 1.86	+0.58± 2.32	-0.20± 1.59	+0.40	CHM
CHR	surface-flask	NOAA	Republic of Kiribati	1°42'N, 157° 9'W, 0 masl	450	+0.75	+0.17	-0.38± 0.55	-0.23± 0.49	-0.45± 0.58	+0.86	CHR
CIB	surface-flask	NOAA	Spain	41°49'N, 4°56'W, 845 masl	193	+2.50	+3.19	+0.33± 1.80	+0.31± 1.57	+0.17± 1.70	+0.67	CIB
CMA	aircraft-pfp	NOAA	United States	38°50'N, 74°19'W, 0 masl	1639	+1000.00	+2.67	+0.42± 2.99	+0.60± 4.05	+0.44± 2.11	-99.00	CMA
CON	aircraft-flask	NIES-MRI		99°60'S, 999°60'W, -9999 masl	2088	+1000.00	+0.16	+0.06± 0.74	+0.27± 0.67	-0.05± 0.72	-99.00	CON
CPS	surface-insitu	EC	Canada	49°49'N, 74°59'W, 381 masl	329	+1000.00	+3.81	+1.09± 3.74	+3.17± 4.54	+0.15± 2.07	-99.00	CPS
CPT	surface-flask	NOAA	South Africa	34°21'S, 18°29'E, 230 masl	140	+0.75	+0.28	-0.25± 0.72	+0.01± 0.62	-0.51± 0.75	+1.13	CPT
Site code	**Sampling Type**	**Lab.**	**Country**	**Lat, Lon, Elev. (m ASL)**	**No. Obs. Avail.**	**√R (µmol mol⁻¹)**	**√HPH (µmol mol⁻¹)**	**H(x)-y (µmol mol⁻¹)**	**H(x)-y (JJAS) (µmol mol⁻¹)**	**H(x)-y (NDJFMA) (µmol mol⁻¹)**	**Inn. X^2**	**Site code**
CPT	surface-insitu	SAWS	South Africa	34°21'S, 18°29'E, 230 masl	2671	+1000.00	+0.42	-0.12± 0.76	+0.35± 0.69	-0.38± 0.62	-99.00	CPT
CRI	surface-flask	CSIRO	India	15° 5'N, 73°50'E, 60 masl	102	+1000.00	+7.58	-3.45± 6.78	-0.15± 4.54	-6.80± 7.43	-99.00	CRI
CRZ	surface-flask	NOAA	France	46°26'S, 51°51'E, 197 masl	494	+0.50	+0.15	+0.18± 0.30	+0.33± 0.26	+0.05± 0.28	+0.54	CRZ
CYA	surface-flask	CSIRO	Australia	66°17'S, 110°31'E, 51 masl	230	+0.50	+0.10	+0.03± 0.28	+0.21± 0.25	-0.11± 0.23	+0.34	CYA
DND	aircraft-pfp	NOAA	United States	47°30'N, 99°14'W, 472 masl	1439	+1000.00	+2.02	+0.43± 2.32	+1.01± 3.54	+0.31± 1.07	-99.00	DND
DRP	shipboard-flask	NOAA	N/A	59° 0'S, 64°41'W, 0 masl	160	+0.50	+0.20	+0.06± 0.34	+0.21± 0.42	-0.03± 0.27	+0.52	DRP
EGB	surface-insitu	EC	Canada	44°14'N, 79°47'W, 251 masl	2450	+3.00	+6.60	+0.07± 2.08	+0.39± 2.31	-0.21± 1.93	+0.48	EGB
EIC	surface-flask	NOAA	Chile	27°10'S, 109°26'W, 47 masl	370	+5.00	+0.12	+0.45± 1.01	+0.87± 0.87	+0.10± 0.93	+0.05	EIC
ESP	aircraft-pfp	NOAA	Canada	49°23'N, 126°33'W, 7 masl	2912	+1000.00	+4.03	+0.12± 3.52	+0.12± 5.22	+0.16± 2.24	-99.00	ESP
ESP	surface-flask	CSIRO	Canada	49°23'N, 126°33'W, 7 masl	9	+1000.00	+0.60	+0.04± 1.31	+0.72± 0.39	-0.93± 1.30	-99.00	ESP

ESP	surface-insitu	EC	Canada	49°23'N, 126°33'W, 7 masl	1260	+4.00	+4.79	-0.02± 2.11	+0.31± 2.43	+0.02± 1.73	+0.28	ESP
EST	surface-insitu	EC	Canada	51°40'N, 110°12'W, 707 masl	962	+3.00	+4.41	+0.23± 2.03	+0.75± 2.51	-0.05± 1.68	+0.62	EST
ETL	aircraft-pfp	NOAA	Canada	54°21'N, 104°59'W, 492 masl	2134	+1000.00	+1.99	+0.34± 1.84	+0.90± 2.60	+0.09± 1.05	-99.00	ETL
ETL	surface-insitu	EC	Canada	54°21'N, 104°59'W, 492 masl	2459	+3.00	+5.76	+0.11± 1.69	+0.39± 2.08	+0.02± 1.41	+0.34	ETL
FIK	surface-flask	LSCE	Greece	35°20'N, 25°40'E, 150 masl	110	+2.50	+1.40	+0.22± 1.86	-0.27± 1.81	+0.56± 1.85	+0.54	FIK
Site code	**Sampling Type**	**Lab.**	**Country**	**Lat, Lon, Elev. (m ASL)**	**No. Obs. Avail.**	**√R (µmol mol⁻¹)**	**√HPH (µmol mol⁻¹)**	**H(x)-y (µmol mol⁻¹)**	**H(x)-y (JJAS) (µmol mol⁻¹)**	**H(x)-y (NDJFMA) (µmol mol⁻¹)**	**Inn. X^2**	**Site code**
FNS	surface-insitu	RUG	Netherlands	54°50'N, 4°44'E, 0 masl	118	+1000.00	+3.19	-0.49± 2.67	-0.15± 2.22	-1.06± 2.82	-99.00	FNS
FSD	surface-insitu	EC	Canada	49°53'N, 81°34'W, 210 masl	3833	+3.00	+4.95	+0.14± 1.80	+0.53± 2.30	-0.08± 1.37	+0.39	FSD
FTL	aircraft-pfp	NOAA	Brazil	3°31'S, 38°17'W, 3 masl	160	+1000.00	+0.21	-0.35± 1.32	+0.23± 1.40	-0.73± 0.74	-99.00	FTL
FWI	aircraft-pfp	NOAA	United States	44°40'N, 90°58'W, 334 masl	378	+1000.00	+3.00	+0.37± 3.10	+0.17± 4.05	+0.67± 2.20	-99.00	FWI
GMI	surface-flask	NOAA	Guam	13°23'N, 144°39'E, 0 masl	788	+0.75	+0.11	+0.19± 0.79	+0.26± 0.93	+0.23± 0.63	+1.21	GMI
GPA	surface-flask	CSIRO	Australia	12°15'S, 131° 3'E, 25 masl	16	+1000.00	+1.30	+2.32± 3.33	+3.68± 4.09	+0.73± 2.03	-99.00	GPA
HAA	aircraft-pfp	NOAA	United States	21°14'N, 158°57'W, 3 masl	1577	+1000.00	+0.12	+0.51± 0.81	+0.54± 0.89	+0.52± 0.66	-99.00	HAA
HBA	surface-flask	NOAA	United Kingdom	75°36'S, 26°13'W, 30 masl	560	+0.50	+0.14	+0.14± 0.25	+0.34± 0.20	+0.01± 0.20	+0.36	HBA
HDP	surface-insitu	NCAR	United States	40°34'N, 111°39'W, 3351 masl	1793	+1.50	+0.43	-0.17± 1.03	-0.38± 1.24	-0.08± 0.86	+0.56	HDP
HEI	surface-insitu	UHEI-IUP	Germany	49°25'N, 8°40'E, 116 masl	4069	+1000.00	+5.07	-5.49±10.82	-2.13± 7.21	-8.02±12.48	-99.00	HEI
HFM	aircraft-pfp	NOAA	United States	42°32'N, 72°10'W, 340 masl	1548	+1000.00	+2.88	+0.72± 3.11	+1.49± 4.70	+0.23± 1.65	-99.00	HFM
HIL	aircraft-pfp	NOAA	United States	40° 4'N, 87°55'W, 201 masl	1784	+1000.00	+2.78	-0.20± 2.59	-0.63± 3.40	+0.15± 1.84	-99.00	HIL
HIP	aircraft-insitu	HU	United States	99°60'S, 999°60'W, -9999 masl	132298	+1000.00	+0.52	-inf± nan	+0.39± 1.29	-inf± nan	-99.00	HIP
HPB	surface-flask	NOAA	Germany	47°48'N, 11° 1'E, 936 masl	317	+5.00	+6.22	+0.18± 4.03	+0.37± 4.33	-0.02± 3.93	+0.61	HPB
HUN	surface-flask	NOAA	Hungary	46°57'N, 16°39'E, 248 masl	597	+1000.00	+7.82	-0.30± 5.41	+0.87± 5.56	-1.06± 5.47	-99.00	HUN
Site code	**Sampling Type**	**Lab.**	**Country**	**Lat, Lon, Elev. (m ASL)**	**No. Obs. Avail.**	**√R (µmol mol⁻¹)**	**√HPH (µmol mol⁻¹)**	**H(x)-y (µmol mol⁻¹)**	**H(x)-y (JJAS) (µmol mol⁻¹)**	**H(x)-y (NDJFMA) (µmol mol⁻¹)**	**Inn. X^2**	**Site code**
HUN	tower-insitu	HMS	Hungary	46°57'N, 16°39'E, 248 masl	3583	+1000.00	+7.66	+0.03± 5.51	+1.94± 4.16	-0.99± 6.11	-99.00	HUN
HUN	tower-insitu	HMS	Hungary	46°57'N, 16°39'E, 248 masl	3350	+3.00	+7.60	+0.02± 2.42	+0.42± 2.43	-0.20± 2.45	+0.80	HUN
HUN	tower-insitu	HMS	Hungary	46°57'N, 16°39'E, 248 masl	3725	+1000.00	+7.65	-0.25± 5.25	+0.98± 3.87	-0.80± 6.03	-99.00	HUN
HUN	tower-insitu	HMS	Hungary	46°57'N, 16°39'E, 248 masl	3784	+1000.00	+7.58	-0.26± 5.05	+0.75± 3.83	-0.67± 5.77	-99.00	HUN
ICE	surface-flask	NOAA	Iceland	63°24'N, 20°17'W, 118 masl	566	+1.50	+0.47	-0.44± 1.15	-0.13± 1.30	-0.60± 1.06	+0.70	ICE
INU	surface-insitu	EC	Canada	68°19'N, 133°32'W, 113 masl	288	+1000.00	+2.96	+0.79± 3.20	+1.59± 3.99	+0.50± 2.08	-99.00	INU
IZO	surface-flask	NOAA	Spain	28°19'N, 16°30'W, 2372 masl	506	+1000.00	+0.17	+0.68± 1.01	+0.80± 1.01	+0.59± 1.02	-99.00	IZO
IZO	surface-insitu	AEMET	Spain	28°19'N, 16°30'W, 2372 masl	4190	+0.75	+0.17	+0.14± 0.68	+0.22± 0.73	+0.08± 0.67	+0.95	IZO
JFJ	surface-insitu	KUP	Switzerland	46°33'N, 7°59'E, 3570 masl	2164	+1.50	+0.76	+0.36± 1.28	+0.45± 1.23	+0.29± 1.32	+0.85	JFJ
JFJ	surface-insitu	EMPA	Switzerland	46°33'N, 7°59'E, 3570 masl	1207	+1000.00	+0.72	+0.16± 1.94	+0.46± 1.54	-0.07± 2.35	-99.00	JFJ
KEY	surface-flask	NOAA	United States	25°40'N, 80° 9'W, 1 masl	422	+2.50	+1.07	-0.02± 1.00	+0.30± 0.92	-0.21± 1.07	+0.17	KEY
KUM	surface-flask	NOAA	United States	19°31'N, 154°49'W, 3 masl	591	+1.50	+0.13	-0.05± 0.94	-0.00± 0.95	-0.02± 0.95	+0.40	KUM
KUM	surface-flask	SIO	United States	19°31'N, 154°49'W, 3 masl	376	+1000.00	+0.12	+0.08± 1.09	+0.05± 1.21	+0.11± 1.09	-99.00	KUM
KZD	surface-flask	NOAA	Kazakhstan	44° 3'N, 76°49'E, 573 masl	371	+2.50	+3.35	-0.18± 2.11	-0.43± 2.22	+0.06± 1.88	+0.81	KZD
KZM	surface-flask	NOAA	Kazakhstan	43°15'N, 77°53'E, 2519 masl	351	+2.50	+0.92	+0.13± 2.25	+0.98± 2.24	-0.66± 1.78	+0.87	KZM
Site code	**Sampling Type**	**Lab.**	**Country**	**Lat, Lon, Elev. (m ASL)**	**No. Obs. Avail.**	**√R (µmol mol⁻¹)**	**√HPH (µmol mol⁻¹)**	**H(x)-y (µmol mol⁻¹)**	**H(x)-y (JJAS) (µmol mol⁻¹)**	**H(x)-y (NDJFMA) (µmol mol⁻¹)**	**Inn. X^2**	**Site code**
LEF	aircraft-pfp	NOAA	United States	45°57'N, 90°16'W, 472 masl	2487	+1000.00	+3.53	-0.05± 2.93	+0.16± 4.10	+0.04± 1.51	-99.00	LEF
LEF	surface-pfp	NOAA	United States	45°57'N, 90°16'W, 472 masl	1350	+1000.00	+5.57	+0.28± 3.28	+1.60± 4.63	-0.16± 2.03	-99.00	LEF
LEF	tower-insitu	NOAA	United States	45°57'N, 90°16'W, 472 masl	2823	+3.00	+5.61	+0.09± 1.85	+0.53± 2.32	-0.06± 1.48	+0.42	LEF
LEF	tower-insitu	NOAA	United States	45°57'N, 90°16'W, 472 masl	2891	+1000.00	+4.96	-0.06± 3.93	+0.56± 5.81	-0.20± 2.18	-99.00	LEF
LJO	surface-flask	SIO	United States	32°54'N, 117°18'W, 10 masl	195	+2.50	+0.96	+3.10± 1.72	+4.10± 1.81	+2.64± 1.46	+2.22	LJO
LLB	surface-flask	NOAA	Canada	54°57'N, 112°27'W, 540 masl	155	+1000.00	+5.85	-0.02± 4.68	+1.16± 6.00	-0.61± 3.87	-99.00	LLB
LLB	surface-insitu	EC	Canada	54°57'N, 112°27'W, 540 masl	1739	+3.00	+4.81	-0.04± 2.21	+0.63± 2.40	-0.41± 2.12	+0.69	LLB
LMP	surface-flask	NOAA	Italy	35°31'N, 12°37'E, 45 masl	291	+1.50	+1.45	+0.29± 1.15	+0.00± 1.21	+0.50± 1.05	+0.67	LMP
LPO	surface-flask	LSCE	France	48°48'N, 3°35'W, 10 masl	187	+2.50	+4.21	-0.11± 1.65	+0.30± 1.87	-0.42± 1.48	+0.47	LPO
LUT	surface-insitu	RUG	Netherlands	53°24'N, 6°21'E, 1 masl	861	+5.00	+9.98	-0.77± 3.50	-0.13± 3.47	-1.23± 3.47	+0.66	LUT
MAA	surface-flask	CSIRO	Australia	67°37'S, 62°52'E, 32 masl	221	+0.50	+0.10	-0.00± 0.27	+0.23± 0.21	-0.13± 0.23	+0.33	MAA
MEX	surface-flask	NOAA	Mexico	18°59'N, 97°19'W, 4464 masl	199	+5.00	+0.45	+0.86± 1.70	+1.53± 1.81	+0.24± 1.05	+0.15	MEX
MHD	surface-flask	NOAA	Ireland	53°20'N, 9°54'W, 5 masl	488	+1.50	+0.70	+0.19± 0.87	+0.60± 0.90	-0.01± 0.79	+0.44	MHD
MID	surface-flask	NOAA	United States	28°13'N, 177°23'W, 11 masl	586	+1.50	+0.22	+0.65± 0.99	+1.17± 1.03	+0.41± 0.88	+0.66	MID
MKN	surface-flask	NOAA	Kenya	0° 4'S, 37°18'E, 3644 masl	138	+2.50	+0.23	+1.64± 1.98	+2.43± 2.19	+1.27± 1.47	+1.08	MKN
Site code	**Sampling Type**	**Lab.**	**Country**	**Lat, Lon, Elev. (m ASL)**	**No. Obs. Avail.**	**√R (µmol mol⁻¹)**	**√HPH (µmol mol⁻¹)**	**H(x)-y (µmol mol⁻¹)**	**H(x)-y (JJAS) (µmol mol⁻¹)**	**H(x)-y (NDJFMA) (µmol mol⁻¹)**	**Inn. X^2**	**Site code**
MLO	surface-flask	NOAA	United States	19°32'N, 155°35'W, 3397 masl	667	+1000.00	+0.12	+0.16± 0.59	+0.16± 0.69	+0.16± 0.53	-99.00	MLO

MLO	surface-flask	CSIRO	United States	19°32'N, 155°35'W, 3397 masl	293	+1000.00	+0.11	+0.23± 0.68	+0.15± 0.62	+0.37± 0.70	-99.00	MLO
MLO	surface-flask	SIO	United States	19°32'N, 155°35'W, 3397 masl	423	+1000.00	+0.11	+0.35± 0.63	+0.28± 0.60	+0.40± 0.69	-99.00	MLO
MLO	surface-insitu	NOAA	United States	19°32'N, 155°35'W, 3397 masl	3794	+0.75	+0.11	+0.21± 0.54	+0.05± 0.52	+0.31± 0.52	+0.65	MLO
MNM	surface-insitu	JMA	Japan	24°17'N, 153°59'E, 8 masl	79922	+1000.00	+0.21	+0.29± 0.74	+0.34± 0.79	+0.37± 0.71	-99.00	MNM
MQA	surface-flask	CSIRO	Australia	54°29'S, 158°58'E, 12 masl	278	+0.50	+0.14	+0.29± 0.48	+0.60± 0.50	+0.08± 0.36	+1.30	MQA
NAT	surface-flask	NOAA	Brazil	5°31'S, 35°16'W, 15 masl	121	+2.50	+0.19	-0.64± 0.99	-0.44± 1.11	-0.73± 0.92	+0.23	NAT
NAT	surface-flask	IPEN	Brazil	5°31'S, 35°16'W, 15 masl	101	+1000.00	+0.17	-0.39± 1.30	-0.38± 1.54	-0.32± 1.00	-99.00	NAT
NHA	aircraft-pfp	NOAA	United States	42°57'N, 70°38'W, 0 masl	2515	+1000.00	+2.52	+0.33± 2.34	+0.55± 3.19	+0.23± 1.81	-99.00	NHA
NMB	surface-flask	NOAA	Namibia	23°35'S, 15° 2'E, 456 masl	249	+1.50	+0.48	-0.10± 1.12	+0.43± 1.00	-0.65± 1.01	+0.67	NMB
NWR	surface-flask	NOAA	United States	40° 3'N, 105°35'W, 3523 masl	575	+1000.00	+0.56	+0.60± 1.39	+1.66± 1.54	+0.04± 0.95	-99.00	NWR
NWR	surface-insitu	NCAR	United States	40° 3'N, 105°35'W, 3523 masl	2071	+2.50	+0.52	-0.24± 1.18	-0.54± 1.37	+0.01± 0.95	+0.27	NWR
OBN	surface-flask	NOAA	Russia	55° 7'N, 36°36'E, 183 masl	132	+5.00	+4.01	+0.61± 3.72	-0.01± 4.26	+0.83± 3.44	+0.55	OBN
OIL	aircraft-pfp	NOAA	United States	41°17'N, 88°56'W, 192 masl	424	+1000.00	+2.43	+0.64± 2.50	+0.68± 3.32	+0.45± 1.26	-99.00	OIL
ORL	aircraft-flask	LSCE	France	47°50'N, 2°30'E, 175 masl	1488	+1000.00	+4.48	-0.11± 4.78	-0.30± 5.87	-0.46± 3.28	-99.00	ORL
Site code	**Sampling Type**	**Lab.**	**Country**	**Lat, Lon, Elev. (m ASL)**	**No. Obs. Avail.**	**√R (µmol mol^{-1})**	**√HPH (µmol mol^{-1})**	**H(x)−y (µmol mol^{-1})**	**H(x)−y (JJAS) (µmol mol^{-1})**	**H(x)−y (NDJFMA) (µmol mol^{-1})**	**Inn. X^2**	**Site code**
OTA	surface-flask	CSIRO	Australia	38°32'S, 142°49'E, 50 masl	71	+1000.00	+0.34	-1.60±20.88	+2.54± 7.79	+0.46± 4.25	-99.00	OTA
OXK	surface-flask	NOAA	Germany	50° 2'N, 11°49'E, 1009 masl	279	+5.00	+2.20	-0.50± 3.43	+0.05± 3.68	-1.09± 3.29	+0.51	OXK
PAL	surface-flask	NOAA	Finland	67°58'N, 24° 7'E, 560 masl	486	+1000.00	+3.02	-0.13± 2.43	+0.27± 3.19	-0.27± 1.81	-99.00	PAL
PAL	surface-insitu	FMI	Finland	67°58'N, 24° 7'E, 560 masl	19652	+1000.00	+3.07	-0.21± 2.28	+0.23± 3.26	-0.25± 1.87	-99.00	PAL
PAL	surface-insitu	FMI	Finland	67°58'N, 24° 7'E, 560 masl	18562	+1000.00	+2.07	+0.08± 1.56	+0.46± 2.43	-0.02± 0.96	-99.00	PAL
PAL	surface-insitu	FMI	Finland	67°58'N, 24° 7'E, 560 masl	62962	+4.00	+2.88	-0.07± 2.02	+0.28± 2.83	-0.15± 1.55	+0.27	PAL
PDM	surface-flask	LSCE	France	42°56'N, 0° 8'E, 2877 masl	306	+2.50	+0.47	-0.26± 1.82	+0.03± 2.04	-0.48± 1.51	+0.56	PDM
PFA	aircraft-pfp	NOAA	United States	65° 4'N, 147°17'W, 210 masl	2839	+1000.00	+1.01	+0.27± 1.73	+0.72± 2.47	+0.14± 1.27	-99.00	PFA
POC	shipboard-flask	NOAA	N/A	99°60'S, 999°60'W, 0 masl	2061	+0.75	+0.33	-inf± nan	+0.16± 0.65	-inf± nan	+0.80	POC
PSA	surface-flask	NOAA	United States	64°55'S, 64° 0'W, 10 masl	622	+0.50	+0.28	+0.01± 0.28	+0.12± 0.26	-0.05± 0.24	+0.33	PSA
PSA	surface-flask	SIO	United States	64°55'S, 64° 0'W, 10 masl	279	+1000.00	+0.27	+0.19± 0.33	+0.36± 0.27	+0.08± 0.30	-99.00	PSA
PTA	surface-flask	NOAA	United States	38°57'N, 123°44'W, 17 masl	376	+5.00	+3.52	-2.17± 3.57	-1.55± 3.76	-2.29± 3.42	+0.68	PTA
RBA	surface-insitu	NCAR	United States	36°28'N, 109° 6'W, 2982 masl	846	+1000.00	+0.42	-0.16± 1.17	-0.47± 1.36	+0.11± 0.92	-99.00	RBA
RPB	surface-flask	NOAA	Barbados	13°10'N, 59°26'W, 15 masl	599	+2.50	+0.30	-0.02± 0.70	+0.50± 0.63	-0.27± 0.58	+0.08	RPB
RTA	aircraft-pfp	NOAA	Cook Islands	21°15'S, 159°50'W, 3 masl	1881	+1000.00	+0.12	-0.02± 0.66	+0.24± 0.52	-0.22± 0.70	-99.00	RTA
Site code	**Sampling Type**	**Lab.**	**Country**	**Lat, Lon, Elev. (m ASL)**	**No. Obs. Avail.**	**√R (µmol mol^{-1})**	**√HPH (µmol mol^{-1})**	**H(x)−y (µmol mol^{-1})**	**H(x)−y (JJAS) (µmol mol^{-1})**	**H(x)−y (NDJFMA) (µmol mol^{-1})**	**Inn. X^2**	**Site code**
RYO	surface-insitu	JMA	Japan	39° 2'N, 141°49'E, 260 masl	49592	+1000.00	+1.68	-0.45± 2.68	+0.01± 4.52	-0.23± 1.67	-99.00	RYO
SAN	aircraft-flask	IPEN	Brazil	2°51'S, 54°57'W, 78 masl	1416	+2.00	+0.87	-0.12± 1.52	+0.35± 1.49	-0.43± 1.51	+1.02	SAN
SAN	aircraft-pfp	NOAA	Brazil	2°51'S, 54°57'W, 78 masl	281	+1000.00	+0.83	-0.31± 3.28	-1.54± 3.90	+0.70± 2.70	-99.00	SAN
SCA	aircraft-pfp	NOAA	United States	32°46'N, 79°33'W, 0 masl	1818	+1000.00	+1.55	+0.12± 2.31	+0.16± 2.56	+0.07± 2.30	-99.00	SCA
SCT	surface-pfp	NOAA	United States	33°24'N, 81°50'W, 115 masl	914	+1000.00	+5.47	-0.78± 3.62	-0.90± 4.08	-0.78± 3.27	-99.00	SCT
SCT	tower-insitu	NOAA	United States	33°24'N, 81°50'W, 115 masl	1138	+3.00	+5.48	-0.26± 2.25	-0.06± 2.47	-0.42± 2.17	+0.55	SCT
SCT	tower-insitu	NOAA	United States	33°24'N, 81°50'W, 115 masl	1186	+1000.00	+6.35	-0.34± 5.36	+0.25± 6.77	-0.97± 4.48	-99.00	SCT
SEY	surface-flask	NOAA	Seychelles	4°41'S, 55°32'E, 2 masl	567	+0.75	+0.19	-0.12± 0.72	+0.11± 0.50	-0.37± 0.81	+0.98	SEY
SGP	aircraft-pfp	NOAA	United States	36°36'N, 97°29'W, 314 masl	3780	+1000.00	+3.16	+0.05± 2.44	-0.13± 3.00	+0.34± 1.60	-99.00	SGP
SGP	surface-flask	NOAA	United States	36°36'N, 97°29'W, 314 masl	533	+1000.00	+5.57	-0.67± 3.51	-1.19± 4.01	-0.04± 2.89	-99.00	SGP
SGP	surface-insitu	LBNL	United States	36°36'N, 97°29'W, 314 masl	3087	+3.00	+5.57	+0.07± 2.17	-0.01± 2.47	+0.15± 2.02	+0.55	SGP
SHM	surface-flask	NOAA	United States	52°43'N, 174° 8'E, 23 masl	414	+2.50	+0.63	+0.00± 2.06	+1.67± 2.53	-0.92± 1.00	+0.81	SHM
SIS	surface-flask	CSIRO	Scotland	60°10'N, 1°10'W, 30 masl	64	+5.00	+0.54	+0.58± 1.12	+1.53± 1.12	+0.10± 0.95	+0.07	SIS
SMO	surface-flask	NOAA	American Samoa	14°15'S, 170°34'W, 42 masl	625	+1000.00	+0.12	-0.12± 0.54	+0.23± 0.37	-0.42± 0.48	-99.00	SMO
SMO	surface-flask	SIO	American Samoa	14°15'S, 170°34'W, 42 masl	292	+1000.00	+0.11	+0.05± 0.68	+0.37± 0.52	-0.22± 0.71	-99.00	SMO
Site code	**Sampling Type**	**Lab.**	**Country**	**Lat, Lon, Elev. (m ASL)**	**No. Obs. Avail.**	**√R (µmol mol^{-1})**	**√HPH (µmol mol^{-1})**	**H(x)−y (µmol mol^{-1})**	**H(x)−y (JJAS) (µmol mol^{-1})**	**H(x)−y (NDJFMA) (µmol mol^{-1})**	**Inn. X^2**	**Site code**
SMO	surface-insitu	NOAA	American Samoa	14°15'S, 170°34'W, 42 masl	3909	+0.75	+0.11	-0.05± 0.51	+0.31± 0.36	-0.36± 0.43	+0.51	SMO
SNP	tower-insitu	NOAA	United States	38°37'N, 78°21'W, 1008 masl	1064	+4.00	+4.50	-0.28± 3.06	+0.86± 3.21	-0.97± 2.73	+0.74	SNP
SNP	tower-insitu	NOAA	United States	38°37'N, 78°21'W, 1008 masl	1097	+1000.00	+4.72	-2.77± 4.67	-4.36± 6.46	-1.84± 3.26	-99.00	SNP
SPL	surface-insitu	NCAR	United States	40°27'N, 106°44'W, 3210 masl	2082	+1.50	+0.52	-0.68± 1.28	-0.74± 1.44	-0.67± 1.18	+1.09	SPL
SPO	surface-flask	NOAA	United States	89°59'S, 24°48'W, 2810 masl	618	+1000.00	+0.10	+0.17± 0.26	+0.41± 0.17	-0.00± 0.19	-99.00	SPO
SPO	surface-flask	CSIRO	United States	89°59'S, 24°48'W, 2810 masl	114	+1000.00	+0.10	+0.02± 0.30	+0.22± 0.25	-0.12± 0.28	-99.00	SPO
SPO	surface-flask	SIO	United States	89°59'S, 24°48'W, 2810 masl	254	+1000.00	+0.09	+0.17± 0.28	+0.42± 0.20	+0.01± 0.22	-99.00	SPO
SPO	surface-insitu	NOAA	United States	89°59'S, 24°48'W, 2810 masl	4566	+0.50	+0.10	+0.08± 0.26	+0.33± 0.18	-0.10± 0.18	+0.34	SPO
STM	surface-flask	NOAA	Norway	66° 0'N, 2° 0'E, 0 masl	767	+1.50	+0.93	+0.18± 1.02	+0.37± 1.13	+0.07± 0.95	+0.57	STM

STR	surface-pfp	NOAA	United States	37°45'N, 122°27'W, 254 masl	1000	+3.00	+2.50	-0.14± 2.46	+0.66± 2.32	-0.62± 2.48	+0.71	STR
SUM	surface-flask	NOAA	Greenland	72°36'N, 38°25'W, 3209 masl	553	+1.50	+0.30	+0.25± 0.81	+0.63± 0.92	+0.03± 0.68	+0.36	SUM
SYO	surface-flask	NOAA	Japan	69° 0'S, 39°35'E, 0 masl	300	+0.50	+0.11	+0.04± 0.26	+0.25± 0.19	-0.11± 0.21	+0.32	SYO
SYO	surface-insitu	NIPR	Japan	69° 0'S, 39°35'E, 0 masl	4303	+1000.00	+0.11	+0.02± 0.23	+0.20± 0.19	-0.11± 0.19	-99.00	SYO
TAP	surface-flask	NOAA	Republic of Korea	36°44'N, 126° 8'E, 16 masl	451	+5.00	+1.88	-0.09± 3.41	+0.70± 4.40	-0.28± 2.45	+0.51	TAP
TDF	surface-flask	NOAA	Argentina	54°51'S, 68°19'W, 12 masl	281	+0.75	+0.21	-0.29± 0.55	-0.27± 0.49	-0.24± 0.54	+0.72	TDF
Site code	**Sampling Type**	**Lab.**	**Country**	**Lat, Lon, Elev. (m ASL)**	**No. Obs. Avail.**	**√R (µmol mol^{-1})**	**√HPH (µmol mol^{-1})**	**H(x)-y (µmol mol^{-1})**	**H(x)-y (JJAS) (µmol mol^{-1})**	**H(x)-y (NDJFMA) (µmol mol^{-1})**	**Inn. X^2**	**Site code**
TGC	aircraft-pfp	NOAA	United States	27°44'N, 96°52'W, 0 masl	1901	+1000.00	+0.98	+0.17± 1.45	+0.16± 1.39	+0.21± 1.35	-99.00	TGC
THD	aircraft-pfp	NOAA	United States	41° 3'N, 124° 9'W, 107 masl	1293	+1000.00	+2.51	+0.46± 2.62	+0.39± 2.07	+0.53± 3.10	-99.00	THD
THD	surface-flask	NOAA	United States	41° 3'N, 124° 9'W, 107 masl	494	+5.00	+2.79	-1.95± 3.46	-2.16± 3.80	-1.63± 3.20	+0.62	THD
TOT	surface-insitu	EC	Canada	43°47'N, 79°28'W, 198 masl	1798	+1000.00	+7.70	-4.31± 8.87	-3.22± 8.33	-4.88± 9.66	-99.00	TOT
TRN	tower-insitu	LSCE	France	47°58'N, 2° 7'E, 131 masl	906	+4.00	+6.30	+0.05± 2.72	+0.57± 2.64	-0.25± 2.75	+0.49	TRN
ULB	aircraft-pfp	NOAA	Mongolia	47°24'N, 106° 0'E, 1350 masl	514	+2.00	+0.92	+0.32± 1.10	+0.46± 1.25	+0.31± 1.10	+0.66	ULB
UTA	surface-flask	NOAA	United States	39°54'N, 113°43'W, 1327 masl	547	+2.50	+1.87	+0.28± 1.88	+1.03± 2.02	-0.28± 1.53	+0.64	UTA
UUM	surface-flask	NOAA	Mongolia	44°27'N, 111° 6'E, 1007 masl	580	+2.50	+1.17	-0.10± 2.36	-0.65± 2.61	+0.37± 2.06	+0.98	UUM
WBI	aircraft-pfp	NOAA	United States	41°43'N, 91°21'W, 241 masl	1459	+1000.00	+3.47	+0.20± 2.81	-0.10± 3.67	+0.51± 1.45	-99.00	WBI
WBI	surface-pfp	NOAA	United States	41°43'N, 91°21'W, 241 masl	1213	+1000.00	+7.47	-0.44± 4.49	-0.05± 6.34	-0.50± 2.74	-99.00	WBI
WBI	tower-insitu	NOAA	United States	41°43'N, 91°21'W, 241 masl	1488	+3.00	+7.47	-0.10± 2.10	+0.28± 2.43	-0.26± 1.89	+0.65	WBI
WBI	tower-insitu	NOAA	United States	41°43'N, 91°21'W, 241 masl	1598	+1000.00	+6.32	-1.00± 4.80	-1.35± 6.70	-0.78± 3.32	-99.00	WBI
WGC	surface-pfp	NOAA	United States	38°16'N, 121°29'W, 0 masl	1149	+1000.00	+5.50	-2.13± 7.63	+1.35± 3.83	-4.68± 9.15	-99.00	WGC
WGC	tower-insitu	NOAA	United States	38°16'N, 121°29'W, 0 masl	1423	+3.00	+4.74	+0.26± 2.77	+0.96± 2.29	+0.08± 3.05	+0.92	WGC
WGC	tower-insitu	NOAA	United States	38°16'N, 121°29'W, 0 masl	1520	+1000.00	+4.52	+1.31± 5.20	+3.09± 4.20	+0.21± 5.48	-99.00	WGC
Site code	**Sampling Type**	**Lab.**	**Country**	**Lat, Lon, Elev. (m ASL)**	**No. Obs. Avail.**	**√R (µmol mol^{-1})**	**√HPH (µmol mol^{-1})**	**H(x)-y (µmol mol^{-1})**	**H(x)-y (JJAS) (µmol mol^{-1})**	**H(x)-y (NDJFMA) (µmol mol^{-1})**	**Inn. X^2**	**Site code**
WIS	surface-flask	NOAA	Israel	30°52'N, 34°47'E, 477 masl	629	+2.50	+0.52	-0.23± 1.92	+0.40± 1.66	-0.47± 1.87	+0.63	WIS
WKT	surface-pfp	NOAA	United States	31°19'N, 97°20'W, 251 masl	1282	+1000.00	+4.06	-0.28± 2.61	-0.10± 2.73	-0.33± 2.42	-99.00	WKT
WKT	tower-insitu	NOAA	United States	31°19'N, 97°20'W, 251 masl	2546	+3.00	+4.03	+0.00± 1.89	+0.07± 1.97	-0.04± 1.84	+0.43	WKT
WKT	tower-insitu	NOAA	United States	31°19'N, 97°20'W, 251 masl	2594	+1000.00	+3.21	-0.41± 3.15	-0.10± 3.64	-0.46± 2.77	-99.00	WKT
WLG	surface-flask	NOAA	Peoples Republic of China	36°17'N, 100°54'E, 3810 masl	484	+1.50	+1.07	+0.12± 1.28	+0.50± 1.36	+0.13± 1.17	+0.83	WLG
WSA	surface-insitu	EC	Canada	43°56'N, 60° 1'W, 5 masl	2921	+3.00	+2.12	+0.09± 1.85	+0.81± 2.35	-0.18± 1.43	+0.41	WSA
YON	surface-insitu	JMA	Japan	24°28'N, 123° 1'E, 30 masl	61473	+1000.00	+0.42	-0.01± 1.73	+0.30± 1.63	+0.04± 1.70	-99.00	YON
ZEP	surface-flask	NOAA	Norway and Sweden	78°54'N, 11°53'E, 474 masl	619	+1.50	+0.55	+0.32± 0.88	+0.44± 1.07	+0.19± 0.77	+0.55	ZEP

3. Further Reading

- **ESRL Carbon Cycle Program**
- **WMO/GAW Report No. 206, 2012** [Note: Requires a few minutes to load]
- **CarboEurope Atmospheres Program**
- **ICOS**

Fossil Fuel Module [go to top]

1. Introduction

Human beings first influenced the carbon cycle through land-use change. Early humans used fire to control animals and later cleared forest for agriculture. Over the last two centuries, following the industrial and technical revolutions and the world population increase, fossil fuel combustion has become the largest anthropogenic source of CO_2. Coal, oil and natural gas combustion indeed are the most common energy sources in both developed and developing countries. Various sectors of the economy rely on fossil fuel combustion: power generation, transportation, residential/commercial building heating, and industrial processes. In 2010, the world emissions of CO_2 from fossil fuel burning, cement manufacturing, and flaring reached 9.2 PgC (one PgC=10^{15} grams of carbon) [**CDIAC**]. The North American (U.S.A, Canada, and Mexico) flux of CO_2 to the atmosphere from fossil fuel burning was 1.7 PgC in 2010, representing 18% of the global total. The International Energy Outlook has projected that the global total source will reach 9.9 PgC in 2020 and 11.3 PgC in 2030 [**DOE**].

2. Detailed Description

The fossil fuel emission inventory used in CarbonTracker Europe is the one constructed for the **CARBONES** project by **USTUTT/IER**. It uses emissions from the **EDGAR 4.2 database** together with country and sector specific time profiles derived by IER. A detailed description of the construction of the product is found **here**.

3. Further Reading

- **CDIAC (Marland et al.) Annual Global and National fluxes**
- **CDIAC (Blasing et al.) Monthly USA fluxes**
- **Energy Information Administration (EIA)**
- **CARBONES project**
- **EDGAR Database**
- **Institut fur Energiewirtschaft und Rationelle Energieanwendung**

TM5 Nested Transport [go to top]

1. Introduction

The link between observations of CO_2 in the atmosphere and the exchange of CO_2 at the Earth's surface is transport in the atmosphere: storm systems, cloud complexes, and weather of all sorts cause winds that transport CO_2 around the world. As a result, local events like fires, forest growth, and ocean upwelling can have impacts at remote locations. To simulate the winds and the weather, CarbonTracker uses sophisticated numerical models that are driven by the daily weather forecasts from the specialized meteorological centers of the world. Since CO_2 does not decay or react in the lower atmosphere, the influence of emissions and uptake in locations such as North America and Europe are ultimately seen in our measurements even at the South Pole! Getting the transport of CO_2 just right is an enormous challenge, and costs us almost 90% of the computer resources for CarbonTracker. To represent the atmospheric transport, we use the Transport Model 5 (**TM5**). This is a community-supported model whose development is shared among many scientific groups with different areas of expertise. TM5 is used for many applications other than CarbonTracker, including forecasting air-quality, studying the dispersion of aerosols in the tropics, tracking biomass burning plumes, and predicting pollution levels that future generations might have to deal with.

2. Detailed Description

TM5 is a global model with two-way nested grids; regions for which high-resolution simulations are desired can be nested in a coarser grid spanning the global domain. The advantage to this approach is that transport simulations can be performed with a regional focus without the need for boundary conditions from other models. Further, this approach allows measurements outside the "zoom" domain to constrain regional fluxes in the data assimilation, and ensures that regional estimates are consistent with global constraints. TM5 is based on the predecessor model TM3, with improvements in the advection scheme, vertical diffusion parameterization, and meteorological preprocessing of the wind fields (Krol et al., 2005). The model is developed and maintained jointly by the **Institute for Marine and Atmospheric Research Utrecht (IMAU, The Netherlands)**, the **Joint Research Centre (JRC, Italy)**, the **Royal Netherlands Meteorological Institute (KNMI, The Netherlands)**, and **NOAA ESRL (USA)**. In CarbonTracker, TM5 separately simulates advection, convection (deep and shallow), and vertical diffusion in the planetary boundary layer and free troposphere.

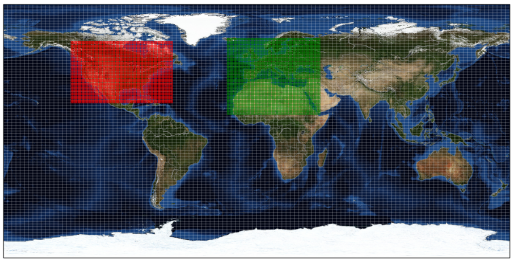

The winds which drive TM5 come from the **European Center for Medium range Weather Forecast (ECMWF)** operational forecast model. This "parent" model currently runs with ~25 km horizontal resolution and 25 layers in the vertical. The carbon dioxide levels predicted by CarbonTracker do not feed back onto these predictions of winds. In contrast to earlier verions of CarbonTracker, we currently use the convection fields directly from ECMWF (whereas before they were calculated using the Tiedtke convection scheme).

For use in TM5, the ECMWF meteorological data are preprocessed into coarser grids. In CarbonTracker Europe, TM5 is run at a global 3x2 degrees resolution with nested regions over Europe (1x1 degrees) and North America (1x1 degree). The grid over Europe is shown in the figure. TM5 runs at an external time step of three hours, but due to the symmetrical operator splitting and the refined resolution in nested grids, processes at the finest scale are repeated every 10 minutes. The vertical resolution of TM5 in CarbonTracker Europe is 25 hybrid sigma-pressure levels, unevenly spaced with more levels near the surface. Approximate heights of the mid-levels (in meters, with a surface pressure of 1012 hPa) are:

Level	Height (m)	Level	Height (m)
1	34.5	14	9076.6
2	111.9	15	10533.3
3	256.9	16	12108.3
4	490.4	17	13874.2
5	826.4	18	15860.1
6	1274.1	19	18093.2
7	1839.0	20	20590.0
8	2524.0	21	24247.3
9	3329.9	22	29859.6
10	4255.6	23	35695.0
11	5298.5	24	42551.5
12	6453.8	25	80000.0
13	7715.4		

3. Further Reading

- **The TM5 model homepage**
- **ECMWF forecast model technical documentation**
- **The NCEP reanalysis meteo data**
- **Peters et al., 2004, JGR paper on transport in TM5**
- **Krol et al., 2005, ACP overview paper of the TM5 model**

Ensemble Data Assimilation [go to top]

1. Introduction

Data assimilation is the name of a process by which observations of the 'state' of a system help to constrain the behavior of the system in time. An example of one of the earliest applications of data assimilation is the system in which the trajectory of a flying rocket is constantly (and rapidly) adjusted based on information of its current position to guide it to its exact final destination. Another example of data assimilation is a weather model that gets updated every few hours with measurements of temperature and other variables, to improve the accuracy of its forecast for the next day, and the next, and the next. Data assimilation is usually a cyclical process, as estimates get refined over time as more observations about the "truth" become available. Mathematically, data assimilation can be done with any number of techniques. For large systems, so-called variational and ensemble techniques have gained most popularity. Because of the size and complexity of the systems studied in most fields, data assimilation projects inevitably include supercomputers that model the known physics of a system. Success in guiding these models in time often depends strongly on the number of observations available to inform on the true system state.

In CarbonTracker, the model that describes the system contains relatively simple descriptions of biospheric and oceanic CO_2 exchange, as well as fossil fuel and fire emissions. In time, we alter the behavior of this model by adjusting a set of parameters as described in the next section.

2. Detailed Description

The four surface flux modules drive instantaneous CO_2 fluxes in CarbonTracker according to:

$$F(x, y, t) = \lambda(x,y,t) \bullet F_{bio}(x, y, t) + \lambda(x,y,t) \bullet F_{oce}(x, y, t) + F_{ff}(x, y, t) + F_{fire}(x, y, t)$$

Where λ represents a set of linear scaling factors applied to the fluxes, to be estimated in the assimilation. These scaling factors are the final product of our assimilation and together with the modules determine the fluxes we present in CarbonTracker. Note that no scaling factors are applied to the fossil fuel and fire modules.

2.1 Land-surface classification

The scaling factors λ are estimated for each week and assumed constant over this period. Each scaling factor is associated with a particular gridbox of the global domain. We chose an approach in which the ocean grid boxes are combined into 30 large basins encompassing large-scale ocean circulation features, as in the TransCom inversion study (e.g. Gurney et al., [2002]). The terrestrial biosphere grid boxes are combined up according to ecosystem type as well as geographical location. Thereto, each of the 11 TransCom land regions contains a maximum of 19 ecosystem types summarized in the table below for Europe.

Ecosystem types considered on 1x1 degree for the terrestrial flux inversions is based on **Olson, [1992]**. Note that we have adjusted the original 29 categories into only 19 regions. This was done mainly to fill the unused categories 16,17, and 18, and to group the similar (from our perspective) categories 23-26+29. The table below shows each vegetation category considered. Percentages indicate the area associated with each category for Europe rounded to one decimal.

Ecosystem Types and area in Europe

category	Olson V 1.3a	%
1	Conifer Forest	14.0
2	Broadleaf Forest	2.5
3	Mixed Forest	8.9
4	Grass/Shrub	8.0
5	Tropical Forest	0.1
6	Scrub/Woods	2.8
7	Semitundra	4.9
8	Fields/Woods/Savanna	6.6
9	Northern Taiga	2.2
10	Forest/Field	11.5
11	Wetland	0.7
12	Deserts	0.1

13	Shrub/Tree/Suc	0.0
14	Crops	22.3
15	Conifer Snowy/Coastal	0.0
16	Wooded tundra	1.6
17	Mangrove	0.0
18	Ice and Polar desert	0.0
19	Water	13.8
99	All	100.0

Each 1x1 degree pixel of our domain was assigned one of the categories above bases on the Olson category that was most prevalent in the 0.5x0.5 degree underlying area.

2.2 Ensemble Size and Localization

The ensemble system used to solve for the scalar multiplication factors is similar to that in Peters et al. [2005] and based on the square root ensemble Kalman filter of Whitaker and Hamill, [2002]. We have restricted the length of the smoother window to only five weeks as we found the derived flux patterns within Europe and North America to be robustly resolved well within that time. We caution the CarbonTracker users that although the North American and European flux results were found to be robust after five weeks, regions of the world with less dense observational coverage (the tropics, Southern Hemisphere, and parts of Asia) are likely to be poorly observable even after more than a month of transport and therefore less robustly resolved. Although longer assimilation windows, or long prior covariance length-scales, could potentially help to constrain larger scale emission totals from such areas, we focus our analysis here on a region more directly constrained by real atmospheric observations.

Ensemble statistics are created from 150 ensemble members, each with its own background CO_2 concentration field to represent the time history (and thus covariances) of the filter. In contrast to our earlier system design, we currently do not apply any localization to the statevector.

2.3 Dynamical Model

In CarbonTracker, the dynamical model is applied to the mean parameter values λ as:

$$\lambda_t^b = (\lambda_{t-2}^a + \lambda_{t-1}^a + \lambda^p) \ / \ 3.0$$

Where "a" refers to analyzed quantities from previous steps, "b" refers to the background values for the new step, and "p" refers to real *a-priori* determined values that are fixed in time and chosen as part of the inversion set-up. Physically, this model describes that parameter values λ for a new time step are chosen as a combination between optimized values from the two previous time steps, and a fixed prior value. This operation is similar to the simple persistence forecast used in Peters et al. [2005], but represents a smoothing over three time steps thus dampening variations in the forecast of λ^b in time. The inclusion of the prior term λ^p acts as a regularization [Baker et al., 2006] and ensures that the parameters in our system will eventually revert back to predetermined prior values when there is no information coming from the observations. Note that our dynamical model equation does not include an error term on the dynamical model, for the simple reason that we don't know the error of this model. This is reflected in the treatment of covariance, which is always set to a prior covariance structure and not forecast with our dynamical model.

2.4 Covariance Structure

Prior values for λ^p are all 1.0 to yield fluxes that are unchanged from their values predicted in our modules. The prior covariance structure P^p describes the magnitude of the uncertainty on each parameter, plus their correlation in space.

In each of these regions on the northern hemisphere, individual λ(x,y) parameters are coupled through an isentropic covariance structure which makes two boxes i and j at a distance d of each other have a covariance C of

$C = 0.64 \bullet \exp(-d/L)$.

In this formula the covariance length scale L varies across the globe. Over Boral and Temperate North America where the observation network is relatively dense, L=300km, but in Boreal and Temperate Asia the number of observations constrains a much smaller number of parameters individually and we chose L=1000km. In Europe, with its strongly heterogeneous land-use and land management and large volume of observations available we took L=200km. In the rest of the world, the length scale is taken infiniely large, coupling fully all grid boxes and associated λ's in the tropics and southern hemisphere.

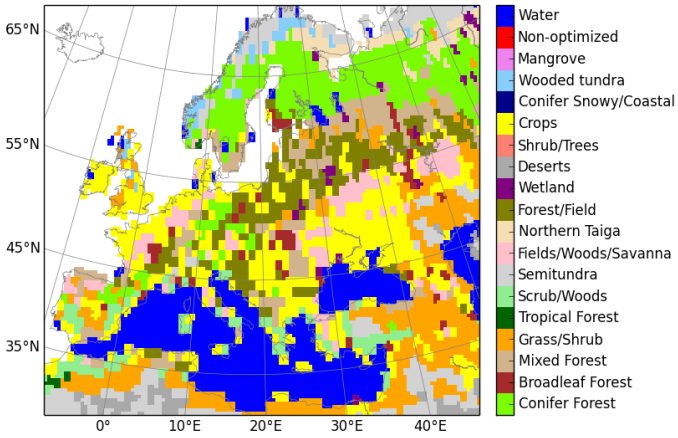

The figure shows ecoregions for Europe (**click here for global land ecoregions**). Note that there is currently no requirement for ecoregions to be contiguous, and a single scaling factor can be applied to the same vegetation type on both sides of a continent.

Theoretically, this approach leads to a total number of 9835 optimizable scaling factors λ each week, but the actual number is smaller since not every ecosystem type is represented in each **TransCom region**, and because we decided not to optimize parameters for ice-covered regions, inland water bodies, and desert. The total flux coming out of these last regions is negligibly small. It is important to note that even though many parameters are available to scale the fluxes, the imposed covariance structure reduces the number of degrees of freedom to about 1100 each week.

Furthermore, all ecosystems *within* tropical **TransCom regions** are coupled decreasing exponentially with distance since we do not believe the current observing network can constrain tropical fluxes on sub-continental scales, and want to prevent large dipoles to occur in the tropics.

In our standard assimilation, the chosen standard deviation is 80% on land parameters, and 40% on ocean parameters. This reflects more prior confidence in the ocean fluxes than in terrestrial fluxes, as is assumed often in inversion studies and partly reflects the lower variability and larger homogeneity of the ocean fluxes. All parameters have the same variance within the land or ocean domain. Because the parameters multiply the net-flux though, ecosystems with larger weekly mean net fluxes have a larger variance in absolute flux magnitude.

3. Further Reading

- **Whitaker and Hamill, 2002 paper**
- **Peters et al., 2005 paper**
- **Olson ecosystem types, data**